Supplementary information for:

Physical Scaling for Predicting Shear Viscosity and Memory Effects of Lithium-Ion Battery Cathode Slurries

Yoshita Gupta[†1] , Qingsong Liu[†1], Jeffrey J. Richards*[1]

[†]: Y.G. and Q.L. contributed equally to this work

[1]. Department of Chemical and Biological Engineering, Northwestern University, Evanston, IL, 60208

*. Authors to whom correspondence should be addressed; electronic mails:

jeffrey.richards@northwestern.edu

Contents

S.1: Conditioning Protocol for Rheo-electric Measurement of Slurries

Hipp et al.[1] and Liu et al.[2] established protocols for conducting rheo-electric measurements of carbon black (CB) suspensions using a three-step process: pre-shear, shear at the specific rate of interest, and post-shear (rest), each lasting 160 second, allowing collecting electric data over a frequency range of 20–10,000,000 Hz. Before testing each shear rate (typically 10 to 14 different rates in an experiment), the sample undergoes a pre-shear at 2500 s^{-1}. This step ensures that every test starts with the same microstructure, enabling consistent comparisons across different shear rates. This structural reproducibility is demonstrated for a 3.5 wt% CB suspension with a polyvinylidene difluoride (PVDF) 761 (or HP) concentration of 36.3 mg/mL, as shown in the Nyquist plot in Fig S1a Here, the consistent real and imaginary impedance values at all pre-shears confirm that the sample starts from an identical structural baseline before each shear rate test. As the electrical measurements are a sensitive probe to the microstructure, the consistent real and imaginary impedance values at all pre-shears tested confirm that the sample starts from an identical structural baseline before each shear rate test.

We applied a similar protocol to the same CB/PVDF suspension containing 10 wt% active material NMC. However, the Nyquist plot in Fig. S1b reveals that the pre-shear step at 2500 s^{-1} failed to produce consistent real and imaginary impedance values across all pre shear cycles for this suspension and therefore prevents accurate measurement of shear-dependent changes from a common reference point.

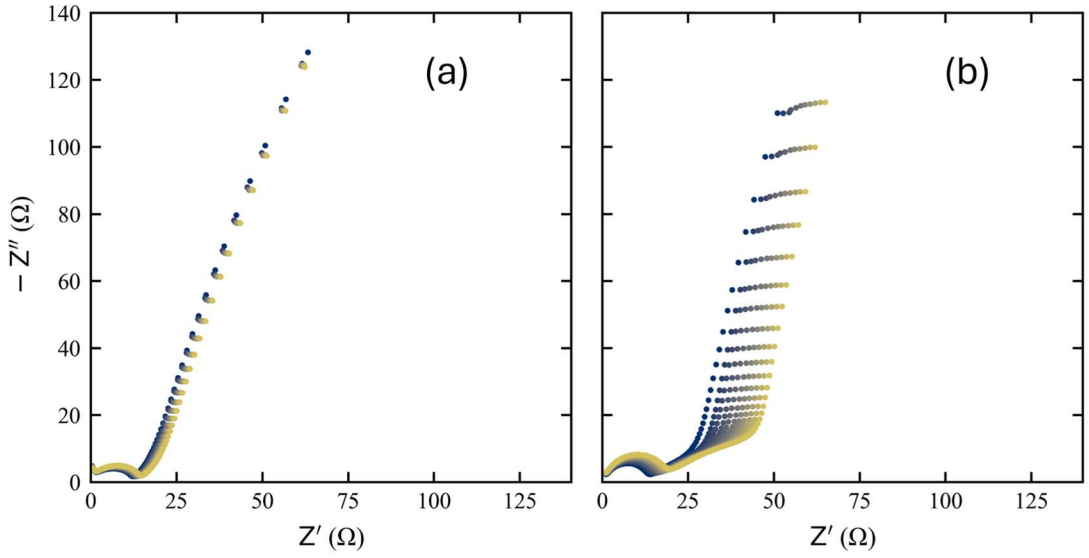

Figure S.1 Nyquist plots for 3.5 wt% CB suspensions in 36.3 mg/mL PVDF 761 under pre-shear conditions at 2500 1/s tested before rheo-electric measurement at a specific shear : (a) Observed consistent real (Z') and imaginary ($-Z''$) impedance values across all pre-shear steps, confirming reproducible microstructure or a common starting point before each shear rate measurement. (b) Suspension with 10 wt% NMC, showing significant variations in impedance values across pre shear cycles, indicating changing microstructure at the same pre-shear, preventing common starting point which hinders accurate shear-dependent measurements.

To address this issue and establish a reproducible reference microstructure at the pre-shear stage, we introduced an additional conditioning step into our protocol, implemented before the rheo-electric measurements. This step involved alternating a high shear rate of 2500 1/s and a low shear rate of 100 1/s, each applied for 160 seconds, repeated over 22 cycles. This conditioning protocol eliminates any mixing memory[3] from the Thinky mixer and achieves a structure that can be reproduced across all preshear tests. High shear rates can break down large structures or agglomerates, while lower shear rates allow for the rearrangement of smaller structures into a more uniform configuration. Fig. S2a demonstrates the impedance values of the suspension measured at every 2500 1/s in the conditioning experiment. The initial cycles displayed significant change in impedance values, the last 7 cycles demonstrated consistency as shown in Fig. S2b, confirming that this conditioning step successfully established a reproducible microstructure.

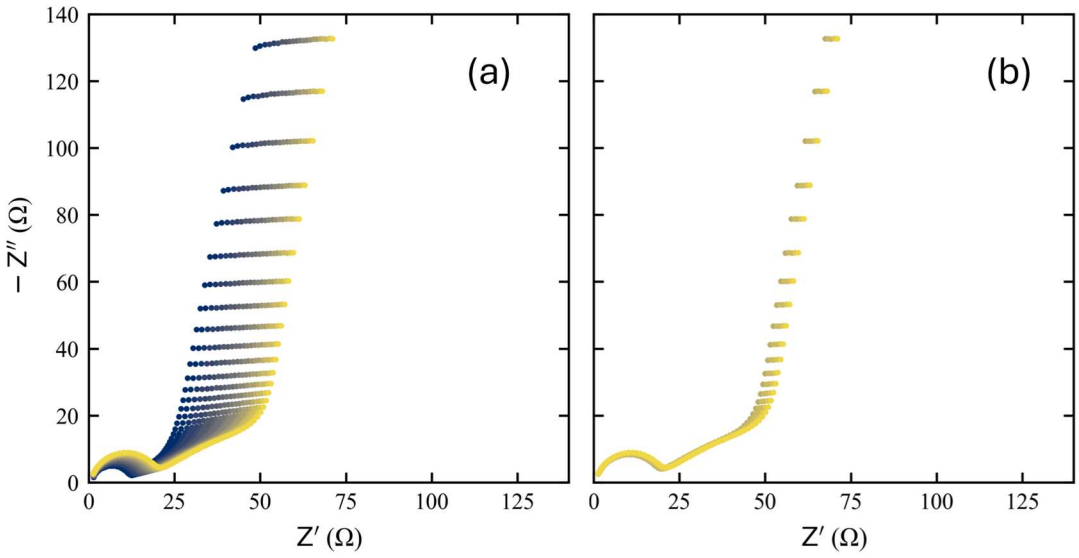

Figure S.2 Nyquist plots with the imaginary impedance ($-Z'$) versus real impedance (Z') for conditioning of 3.5 wt% CB 36.6 mg/mL PVDF 761 with 10wt% NMC in NMP. (a) Impedance measured at 2500 1/s across 22 cycles, highlighting major shifting in microstructure (b) The last 7 cycles of conditioning, showing eventually stabilized and consistent impedance measurements across the frequency range. These measurements demonstrate the elimination of mixing memory and establishment of a reproducible microstructure.

To further validate microstructure reproducibility at the pre-shear stage, we conducted standard rheo-electric measurements after the conditioning step. As shown in Fig. S3, within 10%, and the impedance plots demonstrated similar values at any given frequency across all pre-shear steps at 2500 s^{-1}, confirming a consistent microstructure baseline.

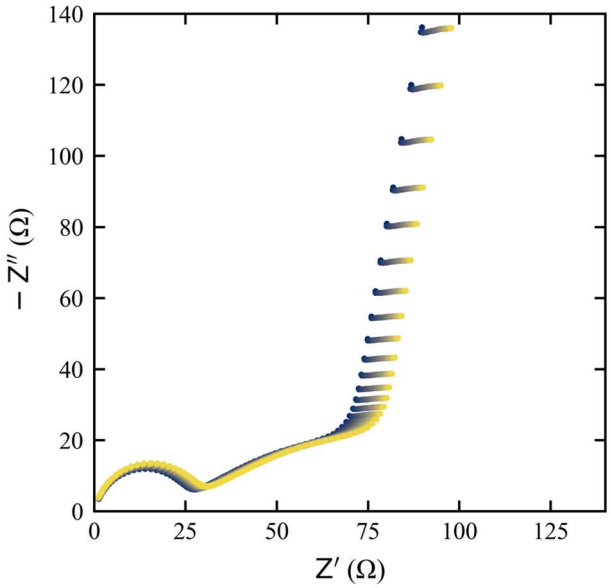

Figure S.3 Nyquist plots for 3.5 wt% CB suspensions in 36.3 mg/mL PVDF 761 and 10 wt% NMC under pre-shear conditions at 2500 1/s before testing a specific shear : Observed consistent real (Z') and imaginary ($-Z''$) impedance values across all pre-shear steps, confirming reproducible microstructure or a common starting point before each shear rate measurement.

For all suspensions containing AM, this revised protocol was adopted, incorporating the conditioning step with alternating shear rates of 2500 s^{-1} and 100 s^{-1} for 160 seconds each, repeated over 22 cycles. After conditioning, rheo-electric measurements were performed, starting with a pre-shear at 2500 s^{-1}, followed by shearing at the desired rate (between 1 and 2500 s^{-1}), and concluding with a quiescent phase. The pre-shear and shear steps each last 160 seconds and the post-shear step entails a 50-second resting period for structure rearrangements and then a 160-second measurement period. This three-step measurement process was repeated for each shear rate tested, ensuring a consistent starting microstructure for every test.

S.2: Scaling of Relative Viscosity with the Mason Number and Effects of Confinement

Fig. S4a presents the relative viscosity normalized against the modified fluid Mason Number Mn_f following the approach reported by Liu et al.[2] for PVDF/CB suspensions. Their analysis demonstrated a successful collapse of relative viscosity as a function of Mn_f , which we replicated and extended here to include non-Brownian NMC particles in PVDF-CB suspensions. We observed that the collapse is not successful as the y-axis fails to account for the contribution of NMC to thee compositional viscosity which changes across different formulations.

In addition, the presence of NMC might induce an confinement effect which modifies the local shea rate. Brady and Bossis[4] highlight the importance of confinement effects in such systems, and define a confinement factor, which is $\left(1-\left(\frac{\phi_{NMC}}{\phi_{max}}\right)^{0.5}\right)^{-1}$, where ϕ_{NMC} is the volume fraction of NMC particles, and ϕ_{max} is the maximum packing fraction (generally taken as 0.64 for spheres). In Figure S.4(b), we included the confinement factor as a correction to the Mn_f to account for the additional shear effects caused by NMC particles. Even with this adjustment, the normalized viscosity data has minimal changes, showing that the confinement factor has only a small impact under these experimental conditions.

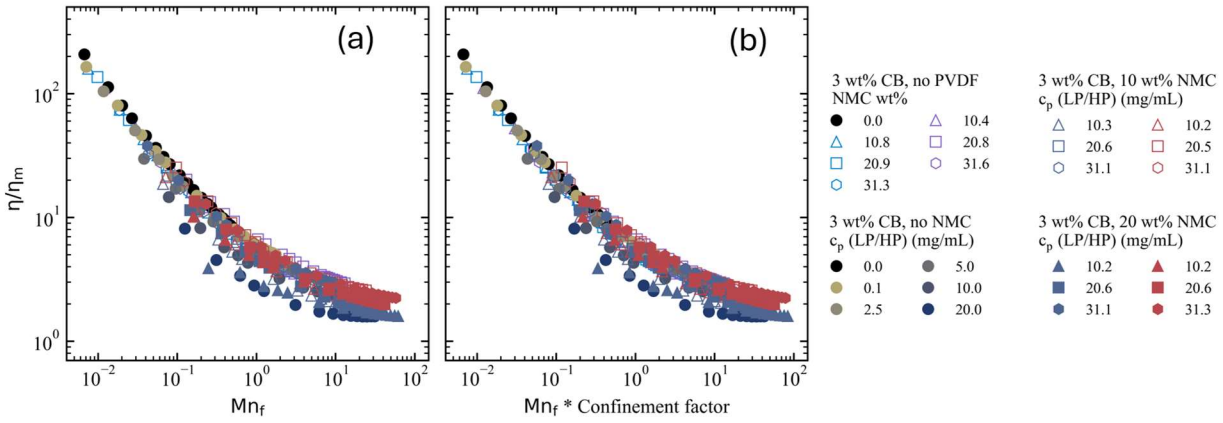

Figure S.4 (a) Relative viscosity normalized against the modified fluid Mason Number Mn_f for 3 wt% CB suspensions in varying PVDF and NMC concentrations. The collapse of viscosity proves the reliability of using Mn_f in describing CB agglomerate behavior under shear in the presence of NMC. (b) Incorporating a confinement factor to Mn_f, accounting for local shear modifications by non-Brownian NMC particles, shows minimal deviation in the viscosity collapse.

S.3: Rheology Measurements of CB/PVDF/NMC Slurries

The Herschel-Bulkley model fit parameters are presented in the table below. In the main text, we discussed the observed trends in yield stress, critical shear rate, and power-law index as functions of NMC weight percent and polymer loading. Specifically, we highlighted the significant reduction in yield stress with increasing NMC concentration in neat CB/NMP suspensions and how the addition of PVDF restores the yield stress and alters the flow behavior. These values are essential for understanding the combined effects of NMC loading, polymer concentration, and polymer molecular weight on the rheological properties at fixed 3 wt% CB in the suspension.

Table S.1 Herschel-Bulkley model fit parameters for 3 wt% CB suspension in various compositions of PVDF/NMC/NMP

Sample	Yield stress (σ_y, Pa)	Error bars	Critical shear rate ($\dot{\gamma}_c$, 1/s)	Error bars	Power law index (n)	Error bars
NMC 0 wt%, HP 0 g/L	7.603	0.015	475.834	2.959	0.642	0.001
NMC 0.1 wt%, HP 0 g/L	2.882	0.019	221.941	4.305	0.740	0.004
NMC 2.5 wt%, HP 0 g/L	1.731	0.012	169.969	2.991	0.778	0.003
NMC 05 wt%, HP 0 g/L	0.535	0.010	68.141	2.290	0.850	0.004
NMC 10 wt%, HP 0 g/L	0.262	0.009	59.990	2.893	0.944	0.004
NMC 20 wt%, HP 0 g/L	0.162	0.017	63.838	7.469	1.000	0.004
NMC 35 wt%, HP 0 g/L	0.058	0.009	20.046	3.340	1.000	0.000
NMC 45 wt%, HP 0 g/L	0.211	0.021	66.215	7.055	1.000	0.001
NMC 0 wt%, HP 10.4 g/L	6.24	0.031	135.243	1.999	0.687	0.002
NMC 0 wt%, HP 20.8 g/L	3.19	0.070	24.429	1.549	0.723	0.006
NMC 0 wt%, HP 31.6 g/L	5.43	0.017	31.508	0.229	0.761	0.001
NMC 0 wt%, LP 10.8 g/L	7.55	0.029	240.680	2.582	0.725	0.002
NMC 0 wt%, LP 20.9 g/L	10.58	0.029	203.144	1.855	0.730	0.002
NMC 0 wt%, LP 31.3 g/L	9.76	0.022	104.753	0.632	0.753	0.001
NMC 10 wt%, HP 10.2 g/L	1.032	0.007	45.504	0.541	0.841	0.001
NMC 10 wt%, HP 20.5 g/L	1.692	0.008	14.832	0.177	0.745	0.001
NMC 10 wt%, HP 31.1 g/L	2.610	0.010	12.923	0.130	0.759	0.001
NMC 10 wt%, LP 10.3 g/L	0.831	0.009	67.199	1.314	0.881	0.002
NMC 10 wt%, LP 20.6 g/L	1.355	0.009	38.065	0.471	0.845	0.001
NMC 10 wt%, LP 31.1 g/L	4.128	0.023	52.987	0.634	0.802	0.001
NMC 20 wt%, HP 10.2 g/L	0.460	0.020	20.153	1.473	0.863	0.005
NMC 20 wt%, HP 20.6 g/L	0.987	0.014	14.442	0.365	0.807	0.002
NMC 20 wt%, HP 31.3 g/L	1.406	0.013	8.382	0.134	0.807	0.001
NMC 20 wt%, LP 10.2 g/L	0.218	0.024	23.157	3.380	0.935	0.006
NMC 20 wt%, LP 20.6 g/L	0.700	0.011	21.749	0.640	0.813	0.002
NMC 20 wt%, LP 31.1 g/L	4.268	0.018	42.880	0.470	0.770	0.001

S.4: Estimating the Fractal Dimension of Super C65 Carbon Black from Rheology

In Fig. 5 presented in the manuscript, we observed a power-law scaling between the differential relative viscosity ($\Delta\eta_r$) and the fluid Mason number, and the fitted power-law slope is -0.93. According to the Krieger- Dougherty equation[5],

$$\Delta\eta_r = \left(1 - \frac{\phi_a}{\phi_m}\right)^{-2.5\phi_m} + 1 \quad \text{(S1)}$$

where ϕ_a is the volume fraction of the agglomerates, and ϕ_m the maximum packing volume fraction. ϕ_a changes as a function of the agglomerate size and can be expanded as

$$\phi_a = \frac{\phi_{eff}}{\phi_p} = \phi_{eff}\left(\frac{R_g}{a}\right)^{3-d_f} \text{ (S2).}$$

ϕ_{eff} is the effective volume fraction, or the volume fraction of primary aggregates which are considered as building blocks here. ϕ_p is the primary aggregate volume fraction inside an agglomerate, or the porosity of the agglomerate, which is defined as $\left(\frac{R_g}{a}\right)^{d_f-3}$. $\frac{R_g}{a}$ is the agglomerate size R_g normalized to the primary aggregate size, and d_f is the fractal dimension. Expanding equation S1 will yield:

$$\Delta\eta_r = \left(1 - \frac{\phi_{eff}}{\phi_m}\left(\frac{R_g}{a}\right)^{3-d_f}\right)^{-2.5\phi_m} + 1 \text{ (S3)}$$

Therefore, the scaling of the $\Delta\eta_r$ and $\frac{R_g}{a}$ for large $\frac{R_g}{a}$ can be estimated as $-2.5\phi_m(3-d_f)$. Assuming ϕ_m to be 0.64 and using the power-law scaling between $\Delta\eta_r$ and Mn_f, $Mn_f \sim \left(\frac{R_g}{a}\right)^{-1.488(3-d_f)}$. Taking the scaling of Mn_f with agglomerate size from Varga et al.[6], (-0.5), the fractal dimension d_f is estimated to be 2.66, similar to the fracal dimension of other CB reported by Hipp et al.[1] .

S.5: Electric Data and Their Fitting

In Fig. S5, an example set of permittivity data for suspensions containing no NMC or little NMC (0.1 wt%) is shown as blue markers, and an example set of permittivity data for other suspensions (containing NMC) is shown as red markers. The real part of the permittivity is shown as filled symbols and the imaginary part unfilled symbols. Both data sets are collected under shear rate of 2500 s^{-1} and represent typical permittivity behaviors of each group. In both data sets, we notice electrode polarization behaviors at low frequencies, and charge relaxation processes at high frequencies, as indicated by the plateaus in the real part. The relaxation process of samples without NMC appears at a lower frequency compared to that shown in samples containing NMC. It is established that such relaxation processes originate from the charge transport between CB agglomerates in our previous publications[2,7]. To avoid over interpreting the permittivity data, we chose to fit only a select range, which includes a constant phase element for the power-law double layer behavior and a Cole-Cole equation and an ideal resistor in parallel for the relaxation process[8]

$$\varepsilon^* = \frac{A}{(i2\pi f)^n} + \frac{1}{\frac{1}{\frac{\Delta\varepsilon}{1+(i2\pi f\tau)^{\alpha}}+\varepsilon_{inf}}+\frac{\kappa}{i2\pi f\varepsilon_0}},$$

where A is the capacitance, n the power-law, $\Delta\varepsilon$ the dielectric strength, α the power law index for the relaxation process, ε_{inf} the infinite permittivity, κ the conductivity of the carbon phase, and ε_0 the free vacuum permittivity. As indicated by the dotted lines for each data set, the fitted frequency ranges are 3×10^3 to 1×10^6 Hz and 3×10^3 to 5×10^6 Hz for no NMC sample group and NMC sample group respectively. To robustly fit the data and obtain the fitting errors, we used a population-based algorithm DREAM[9]. In Fig. 6B, the fitted data and their corresponding fits show excellent agreements. To further confirm the robustness of the algorithm and the equivalent circuit model, we presented the cross-correlation plots of fitted variables in Fig. S6, which only shows strong correlations for variables that are mathematically linked, such as A and n. The detailed fitted parameters and their fitted errors are presented in the attached Excel named 'SI - Electric Data Fits.xlsx'.

In Fig. S7, we presented the ratio of the shear over post-shear conductivity $\kappa_{shear}/\kappa_{post-shear}$ as a function of Mn_f for all formulations tested. The values at the highest Mn_f, or 2500 s^{-1}, were taken to construct the Fig. 6c in the manuscript. We noticed that for all suspensions, the values at low Mn_f remain unchanged; while with increasing Mn_f, this ratio $\kappa_{shear}/\kappa_{post-shea}$ decreases for some of the formulations but not for all of them. This plot highlights both the roles of the formulations and the shear history on tuning the shear dependence of the quiescent structure.

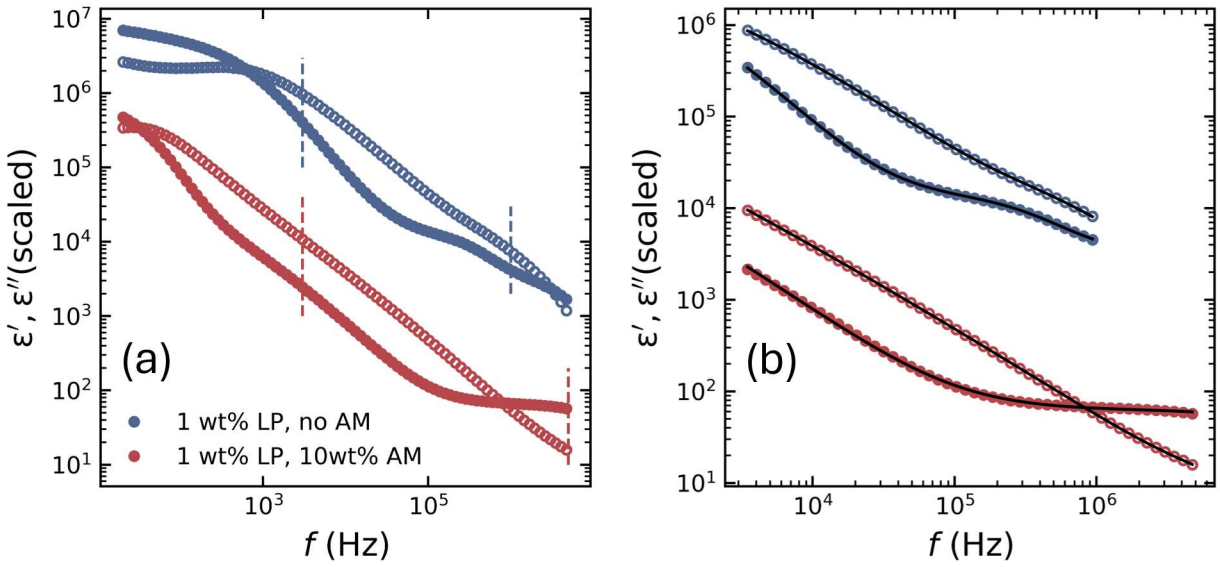

Figure S.5 Example permittivity data and their equivalent circuit fits. (a). Permittivity data (filled, real part; unfilled, imaginary part) of 3 wt% CB and 1 wt% LP suspensions containing no NMC or 10 wt% NMC. The fitted regions are highlighted with dotted lines. (b). The fits are shown along with the data. The equivalent circuit model includes a constant phase element and a relaxation process described by a Cole-Cole equation and an ideal resistor in parallel.

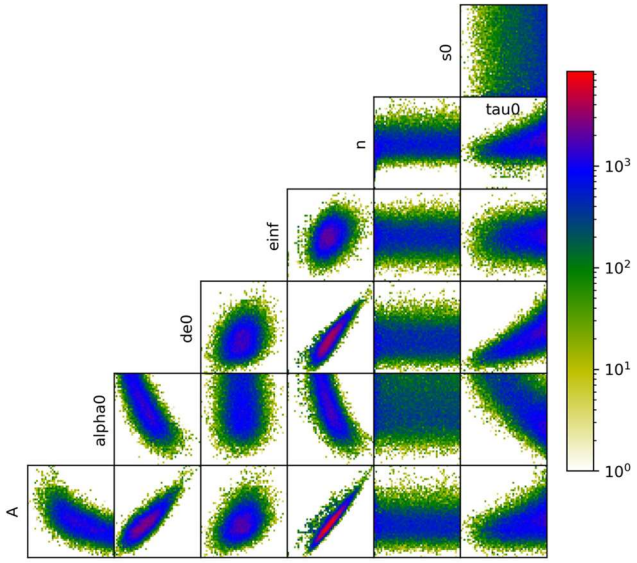

Figure S.6 The cross-correlation plots of fitted parameters for the 3 wt% CB and 1 wt% LP suspension under shear rate of 2500 s^{-1}. Strong correlations are observed only for variables that are mathematically linked. The fitting algorithm is DREAM, a population-based algorithm, via a python package BUMP. The variable κ is represented as S_0 in this plot.

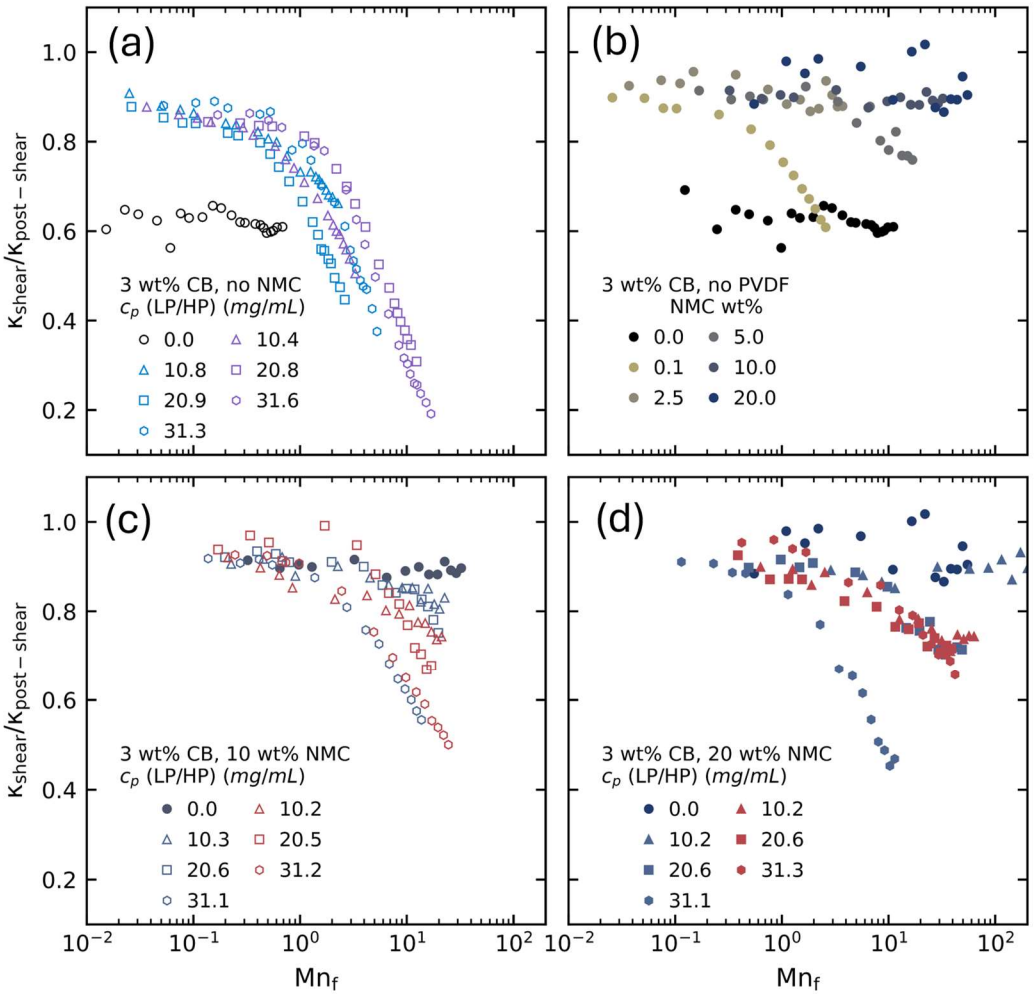

Figure S.7 The ratio of the shear over post-shear carbon-phase conductivity versus Mn_f for suspensions containing 3wt% CB suspensions at different NMC and polymer loadings. (a) 0 wt% NMC in different polymer concentrations of LP and HP (b) no polymer with varying wt% of NMC (b) 10 wt% NMC in different polymer concentrations of LP and HP. (c) 20 wt% NMC in different polymer concentrations of LP and HP.

References

1 J. B. Hipp, J. J. Richards and N. J. Wagner, *J Rheol (N Y N Y)*, 2021, **65**, 145–157.

2 Q. Liu and J. J. Richards, *J Rheol (N Y N Y)*, 2023, **67**, 647–659.

3 J. Mewis and N. J. Wagner, *Colloidal Suspension Rheology*, 2011, **9780521515993**, 1–393.

4 J. Brady and G. Bossis, *J Fluid Mech*, 1985, **155**, 105–129.

5 T. Wang, M. J. Ni, Z. Y. Luo, C. H. Shou and K. F. Cen, *Chinese Science Bulletin*, 2012, **57**, 3644–3651.

6 Z. Varga and J. W. Swan, *J Rheol (N Y N Y)*, 2018, **62**, 405–418.

7 J. B. Hipp, P. Z. Ramos, Q. Liu, N. J. Wagner and J. J. Richards, *Proceedings of the National Academy of Sciences*, 2024, **121**, e2403000121.

8 F. Kramer, *Broadband Dielectric Spectroscopy*, 2003.

9 J. A. Vrugt, C. J. F. Ter Braak, C. G. H. Diks, B. A. Robinson, J. M. Hyman and D. Higdon, *International Journal of Nonlinear Sciences & Numerical Simulation*, 2009, **10**, 273–290.